atmosphere

MDPI

Article

Westerly Variations in the Eastern Tibetan Plateau since the Last Interglacial Revealed by the Grain-Size Records of the Ganzi Loess

Shengli Yang, Jiantao Zhou, Zixuan Chen, Pushuang Li, Chen Wen, Xuechao Xu and Qiong Li *

Key Laboratory of Western China's Environmental System (Ministry of Education), College of Earth and Environmental Sciences, Lanzhou University, Lanzhou 730000, China
* Correspondence: leeqiong@lzu.edu.cn

Abstract: The westerlies play an important role in driving climate change in the Tibetan Plateau (TP). However, little is known about the history of the westerlies in the TP owing to limited observations and a lack of robust reconstructions. The widely distributed eolian loess in the eastern TP is one of the ideal materials to retrieve the intensity history for the westerlies. A detailed grain-size and endmember model analysis (EMMA) on the Ganzi loess sequence located in the eastern TP revealed that the EMMA decomposed the loess grain-size components into four endmembers: EM1 (modal size 1.42 μm) is related to pedogenesis, and EM2 (modal size 7.10 μm) is transported by the westerlies. Silt modes (EM3 and EM4) are transported by the TP winter monsoon or near-surface airflows. The mass accumulation rate (MAR) of EM2 indicated the westerly variations. Combined with the MAR, we reconstructed the history of westerly intensity since the last interglacial period from the Ganzi loess sequence. We found that the intensity of the westerlies showed typical glacial/interglacial variations since the last interglacial period in the eastern TP. The westerly intensity was strong with large fluctuations during the glacial period, whereas it was weak and stable during the Holocene and the last interglacial. The temperature gradient between high and low latitudes caused by changes in insolation and ice volume in the northern hemisphere were the dominant forcing mechanisms for the westerly intensity variations.

Keywords: Tibetan Plateau; loess; grain size; endmember model; the westerlies; last interglacial

Citation: Yang, S.; Zhou, J.; Chen, Z.; Li, P.; Wen, C.; Xu, X.; Li, Q. Westerly Variations in the Eastern Tibetan Plateau since the Last Interglacial Revealed by the Grain-Size Records of the Ganzi Loess. *Atmosphere* **2023**, *14*, 238. https://doi.org/10.3390/atmos14020238

Academic Editor: Alexey V. Eliseev

Received: 5 January 2023
Revised: 17 January 2023
Accepted: 22 January 2023
Published: 25 January 2023

1. Introduction

As a major atmospheric circulation system, the mid-latitude westerlies play a significant role in climatic and environmental evolution, as well as in the evolution of civilization [1,2]. Climate change in the high latitudes of the Northern Hemisphere has a profound impact on the monsoon climate of East Asia, with the Northern Hemisphere westerlies linking the North Atlantic climate and the East Asian summer monsoon (EASM) area [3]. Numerous sources of evidence have suggested that changes in the westerlies were globally synchronous [4], and anthropogenic forcing may cause the poleward migration of the westerlies [5,6].

The Tibetan Plateau (TP) is the largest and highest plateau in the world. Its climate, environment, and vegetation are extremely sensitive to global climate change and are undergoing rapid and pronounced changes [7–11]. The westerlies play an important role in the climate and dust activities in the TP [9,11,12]; further investigation of the changing history of the westerlies is therefore helpful to understand the drivers of environmental change on the TP [13]. Such work is also of great significance to predict future changes in the TP and to protect the so-called Asian water tower [14].

However, current studies on TP westerly intensity variations are mostly focused on the period since the Last Glacial Maximum and the Holocene. The sediment grain-size index in Qinghai Lake shows the westerly variation since 32 ka and suggests that the intensity and

variability in the glacial period were significantly higher than those in the Holocene [15]. Contributions from both the westerlies and the EASM may control the Holocene evolution of moisture conditions in the TP [13,16]. Endmember modeling analysis (EMMA) of the grain size of an eolian sequence in the southern TP suggested that weaker winter westerlies occurred during the Early to Middle Holocene, and stronger winter westerlies occurred in the Middle to Late Holocene [17]. The endmember decomposition grain sizes of the eolian loess–paleosol sections in the Yellow River source area on the northeastern TP indicate that the westerly winds have been inversely correlated with the East Asian summer winds since the Late Pleistocene [18]. The hydrogen isotopes in leaf wax from Jiangcuo-area lake sediments, central TP, indicate that the intensity of the westerlies did not vary much during the Early–Middle Holocene (12–6 ka), but gradually increased since the Middle Holocene [19].

Variations in the westerlies during the last glacial cycle are poorly understood owing to limited observations and a lack of robust reconstructions. It is necessary to investigate more westerly variations at the orbital scale in a more extensive region. Extensive eolian loess deposits in the eastern TP are a key archive to trace past atmospheric circulations [20]. This loess is derived from the TP interior [21], with far-source dust transported by the high-level westerlies and short-distance dust carried by near-surface winds [22,23]. Loess grain size is a direct index of wind strength [24], which is helpful in reconstructing the eolian dust process and atmospheric circulations [25]. Variations in the grain-size distribution of sediments transported by the westerlies can record the evolution of westerly intensity [26], and the grain size of the fine fraction has been used to estimate westerly intensity with Chinese loess [27]. EMMA is a robust and valuable tool as well as a classical quantitative method for grain-size data assessment [28–30], which can identify and quantify processes of sediment generation, transport, and deposition [31,32], EMMA has been widely used in reconstructing westerly evolution in central Asia and the TP [17,18,33,34].

In this study, we conducted a detailed grain-size analysis on the Ganzi loess sequence with good age control and identified a westerlies' component using EMMA. In combination with the dust accumulation rates, the intensity history of the westerlies in the eastern TP has been reconstructed since the last interglacial period, and the possible mechanisms have also been discussed. This result will provide new evidence for further understanding the evolutionary history and proposed mechanism of the westerly variation in the Tibetan Plateau.

2. Materials and Methods

2.1. Study Area and Sampling

Ganzi County is located on the western Sichuan Plateau in the eastern TP where it is affected by the westerlies, the Indian summer monsoon, and the Tibetan Plateau monsoon (Figure 1) [23,35]. The average annual temperature is approximately 6.1 °C, and the annual precipitation is approximately 660 mm, which is concentrated in summer. There are widely distributed eolian loess deposits, especially in the Yalong River terraces. Previous studies have shown that the loess deposits accumulated since approximately 1.13 Ma [36]. The studied XS section (31.37° N, 99.59° E, 3400 m above sea level) is in northeastern Ganzi County, situated on the third terrace at the north bank of the Yalong River. The outcrop is 10 m thick and consists of the last interglacial paleosol (S1), the Holocene paleosol (S0), and a layer of weakly developed paleosol (L1S1). A detailed stratigraphic division and description are given by Yang et al. (2022) [35]. A total of 400 bulk samples were taken at 2.5 cm intervals for grain-size analysis.

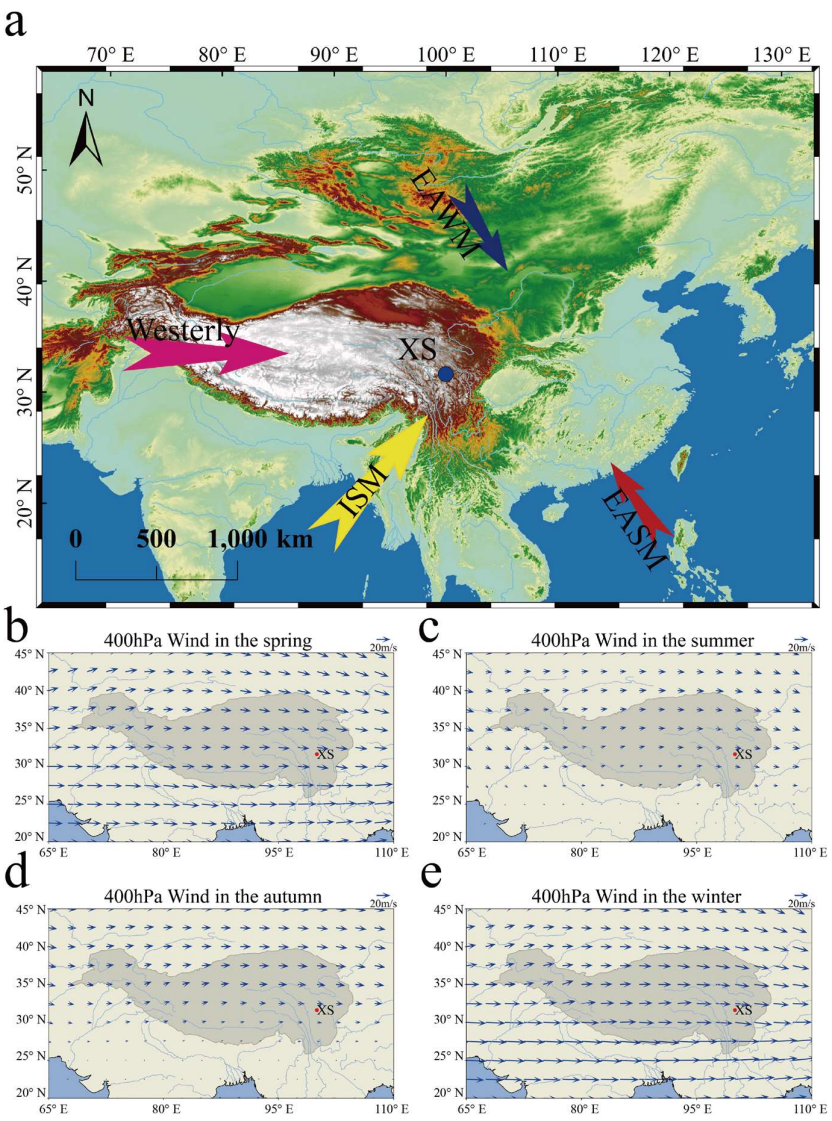

Figure 1. (**a**) The XS section is mainly affected by the westerlies, Indian summer monsoon (ISM), and Tibetan Plateau (TP) monsoon. The red dot is the location of the study site. Wind circulations at the 400 hPa levels in (**b**) spring, (**c**) summer, (**d**) autumn, and (**e**) winter during 1992–2021. The data used here were acquired from https://cds.climate.copernicus.eu/cdsapp#!/dataset/reanalysis-era5-pressure-levels-monthly-means?tab=form (accessed on 1 October 2022).

2.2. Methods

2.2.1. Grain-Size Measurements

Grain-size analyses of bulk loess samples were performed at the Key Laboratory of Western China's Environmental Systems (Ministry of Education), Lanzhou University. The grain size measurements used the methods given by Lu and An [37]. All samples were pretreated with 10% H_2O_2 and HCl to remove organic matter and carbonate, respectively. A 5% dispersing agent of $(NaPO_3)_6$ was added to ultrasonicate for 5 min before measurement. The grain-size distribution was analyzed with a Malvern Mastersizer 2000 laser-diffraction particle-size analyzer, with a measurement range of 0.02–2000 μm, and the measurement error was less than 1%. Finally, the grain-size measurement results of each sample were obtained, and the grain-size distributions are shown in Figure 2a.

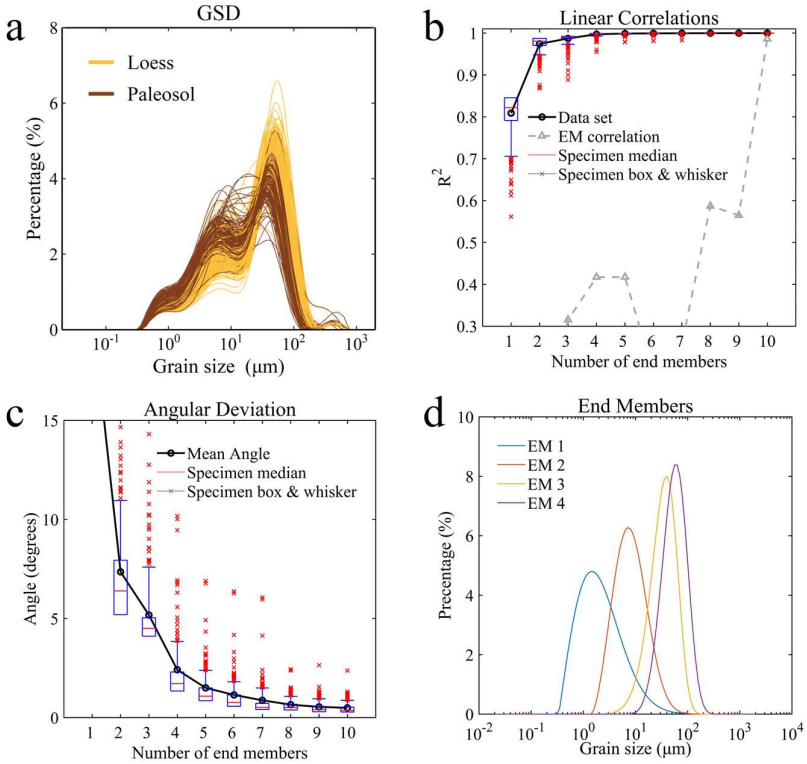

Figure 2. (**a**) Grain-size distribution (GSD) diagrams of all samples, (**b**) linear correlations, (**c**) angular deviations, and (**d**) endmember distributions.

2.2.2. End-Member Analysis

Mathematically, grain-size data EMMA can be understood as follows: The grain-size data of a given sample is regarded as a vector and the grain-size data of a series of samples is a matrix (X), which is composed of multiple vectors. EMMA decomposes X into the product of two matrices, M and B. B is a matrix composed of endmember grain-size distributions, and M is composed of the corresponding proportions of the individual endmembers of each sample. The parametric decomposition method means that the grain-size distribution function of the dust transported by a certain power is specified. That is, given the type of function for each vector in matrix B, the parameters and proportions of the function equation (M) are obtained by inversion. The product of M and B is X′, and there is an error E between X′ and the grain-size matrix X.

In this work, we performed endmember decomposition on grain-size data by the Gen. Weibull function from the AnalySize v.1.2.1 package (https://www.github.com/greigpaterson/AnalySize (accessed on 1 October 2022)) based on MATLAB software [38]. The Gen. Weibull function is one of the most commonly used parametric decomposition functions and an improvement of the Weibull function because it considers the geological background of sediments. The grain-size distribution generally followed the Weibull function, and the Weibull function has a better fit than the log-normal function.

2.2.3. Age Model

Five optically simulated luminescence (OSL) ages obtained from a previous study proved that the bottom age of the XS loess section is 127 ± 6 ka [39]. To reduce the uncertainties in the age constraints, stratigraphic boundary ages were identified for S1, L1L2, L1S1, L1L1, and S0 by correlating the magnetic susceptibility to the corresponding marine isotope stages (MISs) 5 (71–130 ka), MIS 4 (57–71 ka), MIS 3 (29–57 ka), MIS 2 (14–29 ka), and MIS 1 (0–14 ka), respectively [39]. The Bacon age–depth model of the XS section was constructed using R software [40], using the five published OSL ages and four stratigraphic boundary ages (Figure S1).

3. Results

3.1. Grain-Size Results

The grain-size distribution of the XS loess sequence shows a typical log-normal function distribution, with the grain-size distribution concentrated between 2 μm and 70.96 μm and dominated by silt components with less clay and fine sand contents. The mean grain size of loess samples in the XS section is 16.70 μm, whereas the mean grain size of paleosol samples is 14.04 μm. The grain size fluctuates significantly along the depth and is generally fine in the paleosol while coarse in the loess. There are three distinct peaks in the size distribution diagram (Figure 2a) for all XS samples, corresponding roughly to 1 μm, 7 μm, and 50 μm. As shown in Figure 3, clay accounts for a relatively high proportion in the paleosol layers, with the upper and lower quartiles of the proportion accounting for 18.68% and 22.14%, respectively. The proportion is low in the loess layers, with the upper and lower quartiles of the proportion accounting for 15.02% and 19.29%, respectively. There was no significant difference in silt content between the paleosol layers and loess layers, with the upper and lower quartiles of silt content in the paleosol layers accounting for 67.33% to 71.59%, respectively. The sand content is low, with an average proportion of 12.26%. High sand-size fractions occurred in the loess layers with 11.59% to 15.84% in the upper and lower quartiles, while the sand fraction is low in the paleosol layers with 6.88% to 11.98% in the upper and lower quartiles.

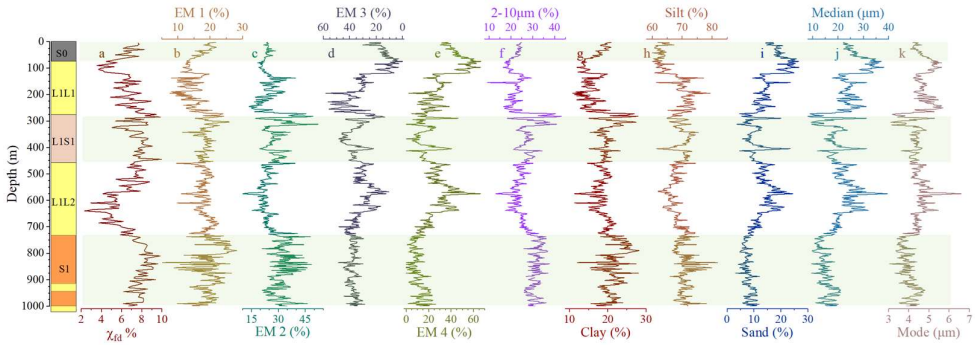

Figure 3. Variation in (**a**) χ_{fd}%, (**b**) clay, (**c**) silt, (**d**) sand, (**e**) the content of the 2–10 μm component, (**f**) EM1, (**g**) EM2, (**h**) EM3, and (**i**) EM4, with (**j**) median grain size and (**k**) mode grain size along the depth.

Along the depth of the XS section, the grain-size records show various degrees of fluctuation in the loess and paleosol layers due to the glacial–interglacial cycles (Figure 3). There were decreasing trends in clay and silt contents (average clay content decreased from 21.72% in S1 to 17.72% in S0; average silt content decreased from 70.61% in S1 to 62.70% in S0) and increasing trends in sand contents (average sand content increased from 7.68% in S1 to 19.58% in S0). The variations in median and mode grain sizes are synchronous, with both showing high values during glacial periods and lower values during the interglacial periods. The variation range of median grain size (31.51 μm) is larger than that of mode grain size (3.54 μm), which means that median grain size is more sensitive to climate conditions.

3.2. EMMA Results

EMMA of XS loess grain-size data was carried out using AnalySize v.1.2.1, and the grain-size matrix was fitted by the Gen. Weibull parametric decomposition function. The linear correlations (R^2), angular deviations (θ), and endmember correlations corresponding to 1–10 endmembers were obtained, which were used to determine the optimal number of endmembers. When the number of endmembers is 4, the linear correlation is 0.99, with an angular deviation of 2.41, and an endmember correlation of 0.41. Based on these three parameters, four endmembers are determined (Figure 2d).

The statistical parameters of the end-member distribution characteristics and the variations in the proportions of the four endmembers (labeled as EM1, EM2, EM3, and EM4) along the depth are shown in Table 1 and Figure 2. EM1 is concentrated between 0.97 μm and 3.63 μm, with a mode size of 1.42 μm, and the proportion is roughly in the range of 10–20%, with moderate fluctuations. The EM2 is between 4.55 μm and 12.19 μm, with a mode size of 7.10 μm, and the proportion is generally lower in glacial periods and higher in interglacial periods. The EM3 varies between 21.60 μm and 47.76 μm, with a mode size of 39.91 μm; EM4 varies between 36.42 μm and 76.27 μm, with a mode size of 56.37 μm. Generally, the proportion of EM3 decreases during the paleosol, while the proportion of EM4 increases. The scatter plot between EM3% and EM4% of all samples showed that there was a significant negative correlation between them (Figure 4e).

Table 1. Statistical parameters of each end member.

	Mode (μm)	Median (μm)	Mean (μm)	Sigma (μm)	Skewness	Kurtosis
EM 1	1.41	1.78	1.92	2.59	0.15	0.96
EM 2	7.10	7.35	7.50	2.03	0.06	0.96
EM 3	39.91	32.96	31.73	1.80	−0.126	1.01
EM 4	56.37	53.32	52.40	1.71	−0.06	0.98

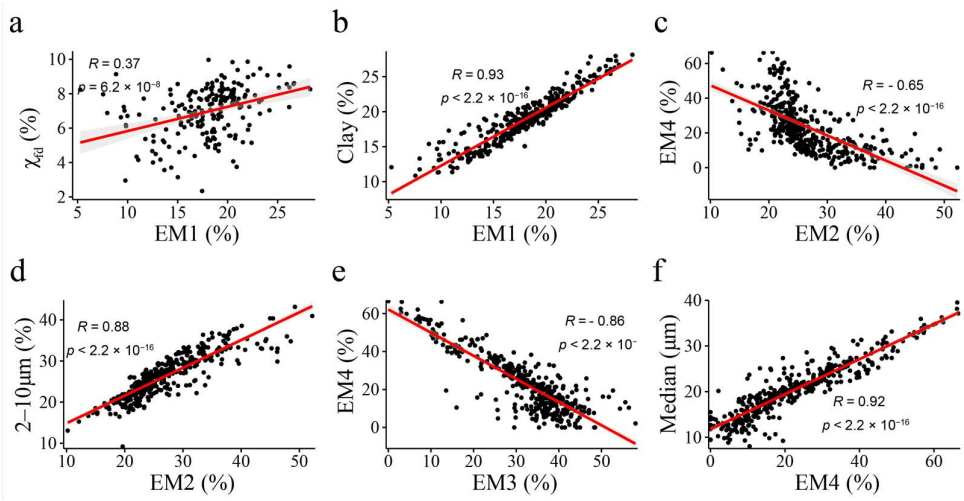

Figure 4. The correlations between (**a**) EM1 and χ_{fd}%, (**b**) EM1 and clay, (**c**) EM2 and EM4, (**d**) EM2 and 2–10 μm%, (**e**) EM3 and EM4, and (**f**) EM4 and median grain size.

4. Discussion

4.1. Paleoclimatic Implications of Endmembers

An area is often affected by winds from multiple systems, each of which contributes dust with different grain-size distribution characteristics [41,42]. Because polymodal sediments are composed of several sedimentary components, the grain-size distribution curve of a single sample consists of a series of overlapping curves corresponding to the various components [43]. EMMA is a method for identifying and quantifying processes of sediment generation, transport, and deposition from the mixed polymodal grain-size distributions of sediments [31]. Since Weltje [29] proposed this method, it has been continuously developed as a robust and reliable tool for grain-size data assessment [28].

Loess grain size is a good indicator for reconstructing dust activity and atmospheric circulation patterns [25,34]. Generally, coarser particles of loess are near-source materials transported by low-level airflow, while fine particles are far-source materials transported by high-level airflow. The dust transport and deposition model proposed by Tsoar and Pye [44] suggested that the coarse dust particles were transported in short-term suspension by lower surface winds, whereas fine particles were transported in long-term suspension over a larger range. Studies on the Loess Plateau showed that the loess median grain size

decreased rapidly from 52 μm to 14 μm within 400 km of the source area, then decreased slowly from 14 μm to 3–6 μm between 400 km and 1000–2000 km, while for 2000–5000 km distances, the median grain size concentrated within 1–3 μm [45].

Current TP dust activities mainly occur in the winter and spring when the westerlies jet shifts to the south of the TP [2,12]. During glaciation, the westerlies shifted southward, which may increase the dust accumulation rate [46]. Thus, the TP loess can well-record the westerlies history. Our EMMA results show that EM1 is mainly clay fraction with grain sizes of 0.97–3.63 μm and median grain size of 1.78 μm. Clay components below 2 μm in size can reflect the strength of pedogenesis [47] and are associated with weathering [48]. The significant positive correlation between EM1 and the clay fraction indicated that EM1 is related to pedogenesis (Figure 4b). The frequency-dependent susceptibility (χ_{fd}%) is a reliable index of pedogenesis and precipitation [20,49] that shows similar variations with EM1—higher in the paleosol layers and lower in the loess layers (Figure 3a). However, the correlation coefficient between EM1% and χ_{fd}% is weak (R = 0.37) (Figure 4a), which may be affected by some long-transported fine particles carried by high-altitude airflow [45].

EM2 is the fine silt fraction ranging from 4.55–12.19 μm, with mode and median grain sizes of 7.10 μm and 7.35 μm, respectively. EM2 is highly correlated with the 2–10 μm% (Figure 4d), and the low kurtosis and large sorting coefficient indicate that it is distant-source material transported by high-altitude winds (Table 1). The particles of 2–10 μm can be transported over long distances by high-level westerlies to any area downwind [50], and the proportion of this component over the section can indicate variations in the strength of the high-level westerlies [25,27]. The low negative correlation between EM2% and EM4% demonstrated that few fine particles were carried in low-level airflow by attaching to large particles or aggregates [27,48] (Figure 4c). In addition, the 30-year ERA5 meteorological data from 1992 to 2021 in the TP demonstrated that the modern wind field in the eastern TP at the 400-hPa level is affected by the westerlies throughout the year with seasonal shifts, especially in winter and spring (Figure 1b–e).

The average content of EM3 (21.60–47.76 μm) is 32% and of EM4 (36.42–76.27 μm) is 23%, with low contents in the paleosols and high contents in the loess. Usually, the coarse fraction is contributed by dust storms generated by low-level airflow [51]. The distribution of modern dust grain size on the Loess Plateau has similar characteristics to EM4 or EM3, mainly near-source material transported by dust storms during spring and summer [52]. Accordingly, we infer that silt mode (EM4 and EM3) was mainly transported by local winds and the TP winter monsoon [12,21,23]. The significant negative correlation between the trends of EM3% and EM4% indicates that they were controlled by an identical mechanism (Figure 4e) [1]. The grain size distribution curves show three distinct peaks (Figure 2): the first two corresponded to the modal size of EM1 and EM2, while the third peak fluctuated to some extent, especially during the glacial period (Figure 3). Therefore, two endmembers (EM3 and EM4) are needed to explain the fluctuation of this maximum peak along the depth. A considerable degree of overlap exists between EM3 and EM4, which may lead to a negative correlation between them. Because the significant fluctuations of the grain size occurred mainly during MIS2 and MIS4 with cold climate conditions, the increased proportions of EM3 and EM4 during these two periods may result in a negative correlation in the MARs. Despite reports on long-transported giant mineral dust particles (>75 μm) [53], it seems that the giant particles have little effect on the Ganzi loess grain size distribution, which is mainly composed of silt and clay. The difference in mode grain size between EM4 and EM3 may be due to transport distance and source region differences. The similar variations and significant correlations of the EM4 and EM3 with median grain size indicate that the EM4 and EM3 were related to the intensity of the TP winter monsoon (Figures 3i–k and 4f) [54].

Therefore, we infer that EM1 was produced by pedogenesis, EM2 was transported by the high-altitude westerlies, and EM3 and EM4 were transported by near-surface winds and the TP winter monsoon, respectively. The transport dynamics of the four endmembers

are basically consistent with previous EMMA studies in loess deposits in different regions (Table S1) [17,18,33].

4.2. The Evolution of the Westerlies over the Tibetan Plateau

EMMA requires that the decomposed endmember ratios 'sum to one' [29]. For a given sample, the variation in the proportion of the primary dynamics in the end member will affect the proportion of the subsidiary dynamics, resulting in a trade-off between them. The mass accumulation rate (MAR) is an ideal index to reflect past dust activities and atmospheric circulation history. Therefore, the dust mass accumulation rate (MAR) of the end-member components is proposed to reconstruct the history of the Asian winter monsoon and westerly wind circulation [33,55,56]. We used the MAR of EM2 to reconstruct the history of the westerlies of the TP. Based on the Bacon age–depth model results and the ratio of EM2 of all samples, we can calculate the MAR of the XS section since the last interglacial (Figure 5b). The MAR was calculated according to the formula: MAR = AR × f × BD [57], where AR is the accumulation rate, which can be obtained by the Bacon age–depth model results [40]; for loess, f = 1; and BD is the dry bulk density. Previous studies showed that the average BD of the XS section is 1.98 g/cm^3 [58].

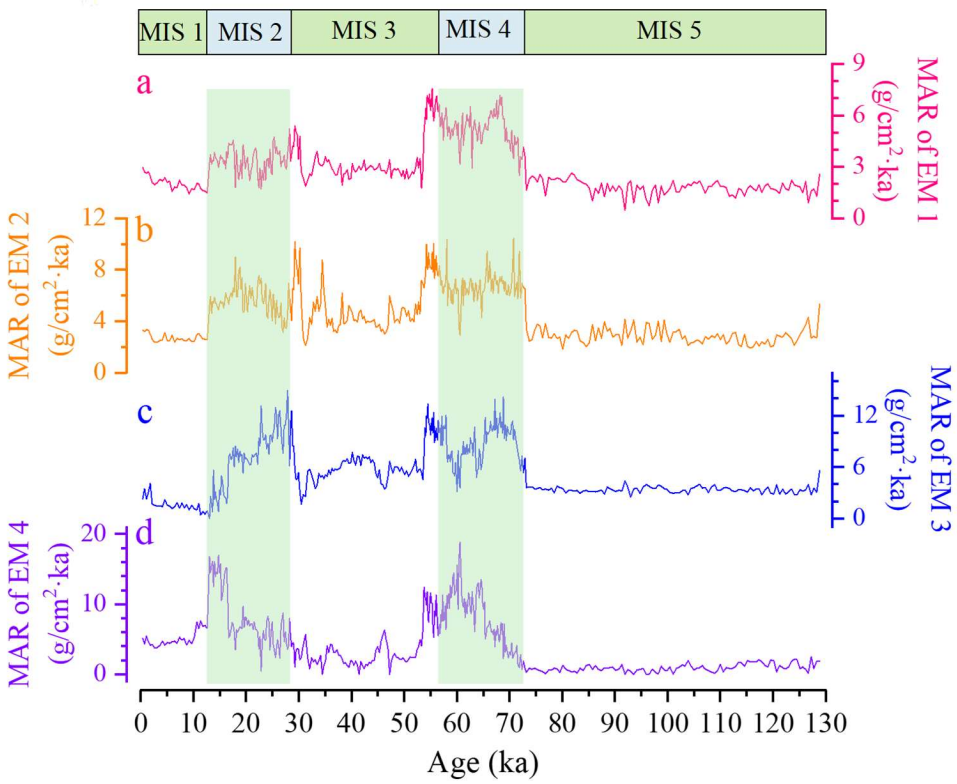

Figure 5. Variations in the mass accumulation rate (MAR) of (**a**) EM1, (**b**) EM2, (**c**) EM3, and (**d**) EM4. MIS: marine isotope stages.

The loess on the eastern TP was mainly transported by the westerly jet and TP monsoon [12,21,23]. The MARs of the four endmembers exhibit an identical trend at the orbital scale since the last interglacial, with high values during MIS2 and MIS4 and low values in MIS5, MIS3, and the Holocene, which indicates that dust of different grain sizes increased and was captured during the glacial period (Figure 5). The similar variations in different endmembers may indicate that the westerly jet and TP monsoon were enhanced during cold stages. The MAR of EM2 represents the dust accumulation contributed by the westerlies, which show distinctive glacial/interglacial variations (Figure 5). During MIS2 and MIS4, the MAR of EM2 was evidently higher than that of the Holocene, MIS3, and the last interglacial. The MAR of EM2 has fluctuated by different degrees in different periods, with

more frequent and higher amplitudes of westerly intensities during glacial periods and less frequent and smaller fluctuations during the interglacial periods. The westerly variability in the Ganzi loess is concordant with previous findings that the westerlies strengthened during glaciation and weakened during interglacial periods [4,59,60]. In addition, our results show that the westerly intensity was weaker and more stable during the last interglacial period and the Holocene. The higher frequency of fluctuations during the cold MIS 2 and MIS 4 can be attributed to the high resolution due to the higher accumulation rates during these periods. The westerly variability during the glacial period is higher than that during the Holocene and last interglacial, which is consistent with results from the Qinghai Lake Basin [15]. During MIS 3, the westerlies showed relatively high variability, which may have been influenced by the rapid millennial-scale climate change [10,61]. High dust accumulation rates at MIS 3 have been reported in the loess deposits in the northeastern TP [62,63] and in the eastern TP [64], which may be affected by atmospheric circulation shifts, wind intensity variations, and dust supply changes [62].

4.3. The Westerly Mechanisms in the Tibetan Plateau

Our records demonstrate that the variability in the westerlies of the TP is consistent with existing study results at the orbital scale. Both climate simulations [59,65] and grain-size indexes [24,55,66] show that the mid-latitude westerlies in the Northern Hemisphere were intensified in the glacial period and shifted southward, whereas they weakened in the warm interglacial periods and migrated poleward [67,68]. The location and intensity of the westerlies are mainly affected by the temperature gradient from the equator to the pole and the extent of the ice sheets [4,10]. The expansion of ice volume in the Northern Hemisphere caused the westerlies to move southward and transported more water vapor to the south and east of the TP from the Late Miocene to the Early Pleistocene [26,69]. Furthermore, the expansion of the Northern Hemisphere ice sheet at the orbital scale not only enhanced the intensity of the westerlies jet but also increased the aridity of the dust source regions in Central Asia [70]. In contrast, a relatively warming climate at high latitudes in Eurasia slows the westerly jet [71].

The findings in this work differed from variations in the westerly intensity in the Holocene. Studies indicated that the westerly winds were strongest during the megathermal event in the Early Holocene of Central Asia and the northeastern TP, showing a good positive correlation between westerly intensity and temperature [33,72,73]. The Tian Shan loess record similarly indicates relatively weak westerly intensities during the Younger Dryas and the Heinrich event H1 cold periods [33], whereas stronger westerly winds occurred during MIS 3, an interglacial epoch in the last glacial period [72]. These differences may be related to the southward shift of the westerly jets during the glaciation leading to the weakening of local westerly wind intensity or the strengthening of the Northern Hemisphere meridional circulation and related weakening of the latitudinal circulation during the glacial period [33].

As shown in Figure 6, the history of the westerlies from the Ganzi loess and Central Asia [66] and the dust mass concentrations in the Greenland ice core [74] have the same trends at the orbital scale, presenting high values during the last glacial period as well as large fluctuations in MIS 3. Eolian dust from Central Asia can be transported to Greenland by high-level westerly winds [75,76], and the dust mass concentrations in Greenland ice cores are a good indicator of westerly intensity. Source studies on snow dust also indicate that TP dust makes an important contribution to Greenland ice core dust [77]. The consistency in the history of the westerlies from the Ganzi loess and the GRIP dust records [74] suggests that the TP is a potential dust source area for the Arctic and that the westerlies are important transport vectors.

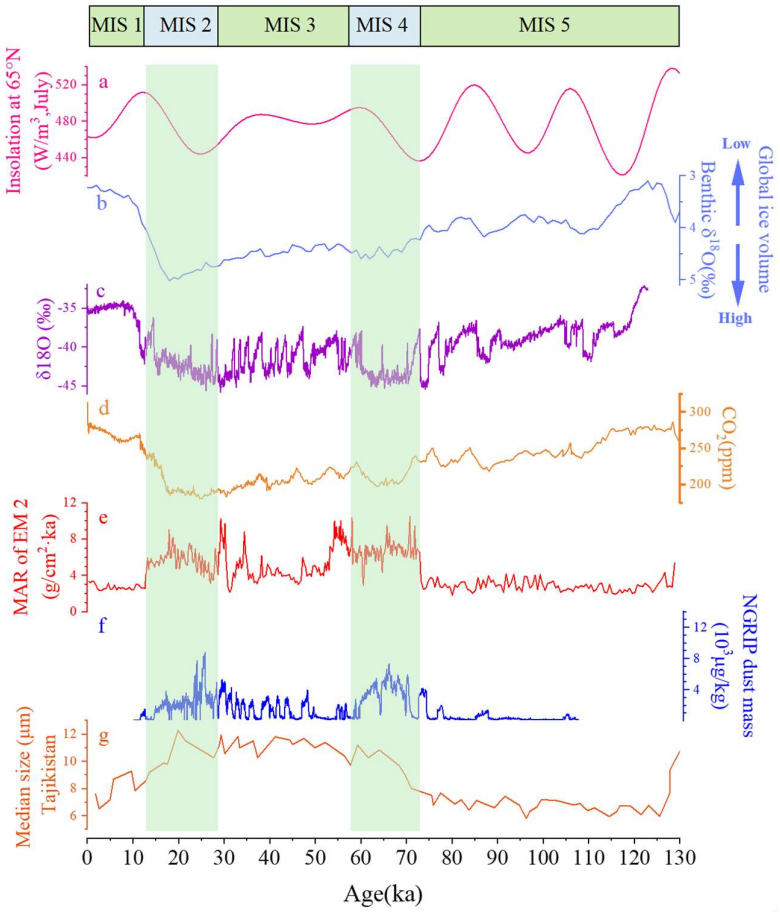

Figure 6. (**a**) July insolation at 65° N in the Northern Hemisphere [78]; (**b**) the LR04 benthic $\delta^{18}O$ record [79]; (**c**) the GISP $\delta^{18}O$ record of Greenland ice [80]; (**d**) atmospheric CO_2 record from Antarctica [81]; (**e**) mass accumulation rate (MAR) of EM2; (**f**) dust mass concentrations from NGRIP ice core [74]; and (**g**) median grain size of the Chashmanigar section in Tajikistan [66]. MIS: marine isotope stages.

The TP westerlies indicated by the MAR of EM2 were strong in the glacial period while weak in the interglacial period, showing a similar trend with the Northern Hemisphere ice volume [79] (Figure 6b), implying that the variations in the westerlies since the last interglacial were mainly driven by ice volume. The influencing factors of climate change at the orbital time scale include solar radiation outside the system as well as ice volume and greenhouse gases inside the system [82]. The summer solar radiation at 65°N during the last glacial period (MIS 2–4) was generally lower than that of the interglacial period, and the low value leads to accumulating ice and snow at high latitudes, which led to ice sheet growth (Figure 6). The variation in CO_2 concentration strengthened the trend of decreasing temperature at high latitudes [83], which further increased the meridional temperature gradient and strengthened the westerly intensity. In addition, the variation of westerly intensity had an important influence on the long-distance transport of dust on the TP [12,46].

5. Conclusions

In this study, we conducted detailed grain-size analyses of a well-dated loess sequence spanning the last interglacial cycle in the eastern TP, to reconstruct the mid-latitude westerly history using endmember model analysis. The EMMA decomposed the Ganzi loess grain-size components into four endmembers: EM1 was related to pedogenesis, and EM2 was transported by the westerlies. Silt modes (EM3 and EM4) were transported by TP winter monsoon or near-surface airflows. Combined with the MAR, we reconstructed the history

of westerly intensity since the last interglacial period from the Ganzi loess sequence. Our results indicate that the westerlies' intensities showed typical glacial/interglacial variations since the last interglacial period in the eastern TP. The westerlies strengthened with large fluctuations during the glacial period, whereas westerly flow was weak and stable during the Holocene and the last interglacial. The temperature gradient between the high and low latitudes caused by changes in insolation and ice volume in the Northern Hemisphere was the dominant influence forcing the variations in the intensity of the westerlies.

Supplementary Materials: The following supporting information can be downloaded at: https://www.mdpi.com/article/10.3390/atmos14020238/s1, Figure S1: Lithology and Bacon age–depth model of the Xinshi (XS) section; Table S1: Comparison of decomposition results in grain-size endmember analysis of loess sediments in different regions. References [17,18,33,56,72,84–89] are cited in the Supplementary Materials.

Author Contributions: Conceptualization, S.Y. and Q.L.; methodology, S.Y.; software, J.Z.; validation, Q.L., S.Y. and J.Z.; formal analysis, S.Y. and J.Z.; investigation, J.Z., Z.C., P.L., C.W. and X.X.; data curation, S.Y. and J.Z.; writing—original draft preparation, S.Y. and J.Z.; writing—review and editing, S.Y. and Q.L.; visualization, J.Z. and Z.C.; funding acquisition, S.Y. All authors have read and agreed to the published version of the manuscript.

Funding: This research was funded by "The Strategic Priority Research Program of the Chinese Academy of Sciences (XDA20090000)", the "National Natural Science Foundation of China (41877447 and 41472147), and the "Second Tibetan Plateau Scientific Expedition and Research Program (STEP) (2019QZKK0602)".

Institutional Review Board Statement: Not applicable.

Informed Consent Statement: Not applicable.

Data Availability Statement: Data is contained within the article or Supplementary Material.

Acknowledgments: The authors are grateful to Li, S., Cheng, T., Liang, M., Hong, M. and Huang, Z. for their help in the field and with laboratory work.

Conflicts of Interest: The authors declare no conflict of interest.

References

1. Chen, F.; Chen, J.; Huang, W.; Chen, S.; Huang, X.; Jin, L.; Jia, J.; Zhang, X.; An, C.; Zhang, J.; et al. Westerlies Asia and monsoonal Asia: Spatiotemporal differences in climate change and possible mechanisms on decadal to sub-orbital timescales. *Earth-Sci. Rev.* **2019**, *192*, 337–354. [CrossRef]
2. Toggweiler, J.R.; Russell, J.L.; Carson, S.R. Midlatitude westerlies, atmospheric CO_2, and climate change during the ice ages. *Paleoceanography* **2006**, *21*, PA2005. [CrossRef]
3. Qu, W.J.; Zhang, X.Y.; Wang, D.; Shen, Z.X.; Mei, F.M.; Cheng, Y.; Yan, L.W. The Important Significance of Westerly Wind Study. *Mar. Geol. Quat. Geol.* **2004**, *24*, 125–132. (In Chinese)
4. Abell, J.T.; Winckler, G.; Anderson, R.F.; Herbert, T.D. Poleward and weakened westerlies during Pliocene warmth. *Nature* **2021**, *589*, 70–75. [CrossRef]
5. Chen, G.; Held, I.M. Phase Speed Spectra and the Recent Poleward Shift of Southern Hemisphere Surface Westerlies. *Geophys. Res. Lett.* **2007**, *34*, L21805. [CrossRef]
6. Yang, H.; Lohmann, G.; Krebs-Kanzow, U.; Ionita, M.; Shi, X.; Sidorenko, D.; Gong, X.; Chen, X.; Gowan, E.J. Poleward Shift of the Major Ocean Gyres Detected in a Warming Climate. *Geophys. Res. Lett.* **2020**, *47*, e2019GL085868. [CrossRef]
7. Yao, T.; Xue, Y.; Chen, D.; Chen, F.; Thompson, L.; Cui, P.; Koike, T.; Lau, W.K.M.; Lettenmaier, D.; Mosbrugger, V.; et al. Recent Third Pole's Rapid Warming Accompanies Cryospheric Melt and Water Cycle Intensification and Interactions between Monsoon and Environment: Multidisciplinary Approach with Observations, Modeling, and Analysis. *Bull. Am. Meteorol. Soc.* **2019**, *100*, 423–444. [CrossRef]
8. Lehnert, L.; Wesche, K.; Trachte, K.; Reudenbach, C.; Bendix, J. Climate variability rather than overstocking causes recent large scale cover changes of Tibetan pastures. *Sci. Rep.* **2016**, *6*, 24367. [CrossRef]
9. Li, W.; Guo, W.; Qiu, B.; Xue, Y.; Hsu, P.-C.; Wei, J. Influence of Tibetan Plateau snow cover on East Asian atmospheric circulation at medium-range time scales. *Nat. Commun.* **2018**, *9*, 4243. [CrossRef]
10. Nagashima, K.; Tada, R.; Matsui, H.; Irino, T.; Tani, A.; Toyoda, S. Orbital- and millennial-scale variations in Asian dust transport path to the Japan Sea. *Palaeogeogr. Palaeoclim. Palaeoecol.* **2007**, *247*, 144–161. [CrossRef]

11. Yao, T.; Masson-Delmotte, V.; Gao, J.; Yu, W.; Yang, X.; Risi, C.; Sturm, C.; Werner, M.; Zhao, H.; He, Y.; et al. A review of climatic controls on $\delta^{18}O$ in precipitation over the Tibetan Plateau: Observations and simulations. *Rev. Geophys.* **2013**, *51*, 525–548. [CrossRef]
12. Fang, X.; Han, Y.; Ma, J.; Song, L.; Yang, S.; Zhang, X. Dust Storms and Loess Accumulation on the Tibetan Plateau: A Case Study of Dust Event on 4 March 2003 in Lhasa. *Chin. Sci. Bull.* **2004**, *49*, 953–960. [CrossRef]
13. Chen, F.; Zhang, J.; Liu, J.; Cao, X.; Hou, J.; Zhu, L.; Xu, X.; Liu, X.; Wang, M.; Wu, D.; et al. Climate change, vegetation history, and landscape responses on the Tibetan Plateau during the Holocene: A comprehensive review. *Quat. Sci. Rev.* **2020**, *243*, 106444. [CrossRef]
14. Immerzeel, W.W.; Van Beek, L.P.H.; Bierkens, M.F.P. Climate change will affect the Asian Water Towers. *Science* **2010**, *328*, 1382–1385. [CrossRef]
15. An, Z.; Colman, S.M.; Zhou, W.; Li, X.; Brown, E.T.; Jull, A.J.T.; Cai, Y.; Huang, Y.; Lu, X.; Chang, H.; et al. Interplay between the Westerlies and Asian monsoon recorded in Lake Qinghai sediments since 32 ka. *Sci. Rep.* **2012**, *2*, 619. [CrossRef]
16. Yang, J.; Xia, D.; Gao, F.; Wang, S.; Li, D.; Fan, Y.; Chen, Z.; Tian, W.; Liu, X.; Sun, X.; et al. Holocene moisture evolution and its response to atmospheric circulation recorded by aeolian deposits in the southern Tibetan Plateau. *Quat. Sci. Rev.* **2021**, *270*, 107169. [CrossRef]
17. Gao, F.; Yang, J.; Wang, S.; Wang, Y.; Li, K.; Wang, F.; Ling, Z.; Xia, D. Variation of the Winter Mid-Latitude Westerlies in the Northern Hemisphere During the Holocene Revealed by Aeolian Deposits in the Southern Tibetan Plateau. *Quat. Res.* **2022**, *107*, 104–112. [CrossRef]
18. Jia, Y.N.; Zhang, Y.; Huang, C.C.; Wang, N.; Qiu, H.; Wang, H.; Xiao, Q.; Chen, D.; Lin, X.; Zhu, Y.; et al. Late Pleistocene-Holocene Aeolian Loess-Paleosol Sections in the Yellow River Source Area on the Northeast Tibetan Plateau: Chronostratigraphy, Sediment Provenance, and Implications for Paleoclimate Reconstruction. *Catena* **2022**, *208*, 105777. [CrossRef]
19. Xie, H.C. Climate Change Characteristics in the Asian Westerlies Dominated Area Recorded by Geochemical Proxies During Late Quaternary. Ph.D. Thesis, Lanzhou University, Lanzhou, China, 2019.
20. Maher, B.A. Palaeoclimatic records of the loess/palaeosol sequences of the Chinese Loess Plateau. *Quat. Sci. Rev.* **2016**, *154*, 23–84. [CrossRef]
21. Yang, S.; Luo, Y.; Li, Q.; Liu, W.; Chen, Z.; Liu, L.; Liu, X. Comparisons of Topsoil Geochemical Elements from Northwest China and Eastern Tibetan Plateau Identify the Plateau Interior as Tibetan Dust Source. *Sci. Total Environ.* **2021**, *798*, 149240. [CrossRef]
22. Wake, C.P.; Mayewski, P.A.; Li, Z.; Han, J.; Qin, D. Modern eolian dust deposition in central Asia. *Tellus B Chem. Phys. Meteorol.* **1994**, *46*, 220. [CrossRef]
23. Fang, X. The Origin and Provenance of Malan Loess Along the Eastern Margin of Qinghai-Xizang (Tibetan) Plateau and Its Adjacent Area. *Sci. China Ser. B* **1995**, *38*, 876–887.
24. Janecek, T.R.; Rea, D.K. Quaternary Fluctuations in the Northern Hemisphere Trade Winds and Westerlies. *Quat. Res.* **1985**, *24*, 150–163. [CrossRef]
25. Vandenberghe, J. Grain size of fine-grained windblown sediment: A powerful proxy for process identification. *Earth Sci. Rev.* **2013**, *121*, 18–30. [CrossRef]
26. Chang, H.; An, Z.; Wu, F.; Jin, Z.; Liu, W.; Song, Y. A Rb/Sr record of the weathering response to environmental changes in westerly winds across the Tarim Basin in the late Miocene to the early Pleistocene. *Palaeogeogr. Palaeoclim. Palaeoecol.* **2013**, *386*, 364–373. [CrossRef]
27. Sun, D.; Bloemendal, J.; Rea, D.K.; An, Z.; Vandenberghe, J.; Lu, H.; Su, R.; Liu, T. Bimodal Grain-Size Distribution of Chinese Loess, and Its Palaeoclimatic Implications. *Catena* **2004**, *55*, 325–340. [CrossRef]
28. Dietze, E.; Maussion, F.; Ahlborn, M.; Diekmann, B.; Hartmann, K.; Henkel, K.; Kasper, T.; Lockot, G.; Opitz, S.; Haberzettl, T. Sediment transport processes across the Tibetan Plateau inferred from robust grain-size end members in lake sediments. *Clim. Past* **2014**, *10*, 91–106. [CrossRef]
29. Weltje, G.J. End-member modeling of compositional data: Numerical-statistical algorithms for solving the explicit mixing problem. *J. Int. Assoc. Math. Geol.* **1997**, *29*, 503–549. [CrossRef]
30. Li, Y.; Song, Y.; Fitzsimmons, K.E.; Chang, H.; Orozbaev, R.; Li, X. Eolian dust dispersal patterns since the last glacial period in eastern Central Asia: Insights from a loess-paleosol sequence in the Ili Basin. *Clim. Past* **2018**, *14*, 271–286. [CrossRef]
31. Dietze, M.; Schulte, P.; Dietze, E. Application of end-member modelling to grain-size data: Constraints and limitations. *Sedimentology* **2021**, *69*, 845–863. [CrossRef]
32. Li, Y.; Song, Y.; Fitzsimmons, K.E.; Chen, X.; Wang, Q.; Sun, H.; Zhang, Z. New Evidence for the Provenance and Formation of Loess Deposits in the Ili River Basin, Arid Central Asia. *Aeolian Res.* **2018**, *35*, 1–8. [CrossRef]
33. Jia, J.; Liu, H.; Gao, F.; Xia, D. Variations in the westerlies in Central Asia since 16 ka recorded by a loess section from the Tien Shan Mountains. *Palaeogeogr. Palaeoclimatol. Palaeoecol.* **2018**, *504*, 156–161. [CrossRef]
34. Li, Y.; Song, Y.; Fitzsimmons, K.E.; Dave, A.K.; Liu, Y.; Zong, X.; Sun, H.; Liu, H.; Orozbaev, R. Investigating Potential Links between Fine-Grained Components in Loess and Westerly Airflow: Evidence from East and Central Asia. *Front. Earth Sci.* **2022**, *10*, 901629. [CrossRef]
35. Yang, S.; Chen, Z.; Chen, H.; Luo, Y.; Liu, L.; Liu, X.; Li, Q.; Zhou, J.; Li, P. Magnetic Properties of the Ganzi Loess and Their Implications for Precipitation History in the Eastern Tibetan Plateau Since the Last Interglacial. *Paleoceanogr.* **2022**, *37*, e2021PA004322. [CrossRef]

36. Yan, M.; Fang, X.; Chen, S.; Yang, S.; Lü, L.; Li, J.; An, Z. Pleistocene magnetic susceptibility and paleomagnetism of the Tibetan loess and its implications on large climatic change events. *Sci. China Ser. D Earth Sci.* **2001**, *44*, 227–232. [CrossRef]
37. Lu, H.; An, Z. Pretreated methods on loess-palaeosol samples granulometry. *Chin. Sci. Bull.* **1998**, *43*, 237–240. [CrossRef]
38. Paterson, G.A.; Heslop, D. New methods for unmixing sediment grain size data. *Geochem. Geophys. Geosyst.* **2015**, *16*, 4494–4506. [CrossRef]
39. Yang, S.; Liu, L.; Chen, H.; Tang, G.; Luo, Y.; Liu, N.; Cheng, T.; Li, D. Variability and environmental significance of organic carbon isotopes in Ganzi loess since the last interglacial on the eastern Tibetan Plateau. *Catena* **2020**, *196*, 104866. [CrossRef]
40. Blaauw, M.; Christen, J.A. Flexible paleoclimate age-depth models using an autoregressive gamma process. *Bayesian Anal.* **2011**, *6*, 457–474. [CrossRef]
41. Vandenberghe, J.; Lu, H.; Sun, D.; van Huissteden, J.; Konert, M. The late Miocene and Pliocene climate in East Asia as recorded by grain size and magnetic susceptibility of the Red Clay deposits (Chinese Loess Plateau). *Palaeogeogr. Palaeoclim. Palaeoecol.* **2004**, *204*, 239–255. [CrossRef]
42. Prins, M.A.; Weltje, G.J. End-Member Modeling of Siliciclastic Grain-Size Distributionsthe Late Quaternary Record of Eolian and Fluvial Sediment Supply to the Arabian Sea and Its Paleoclimatic Significance. In *Numerical Experiments in StratigraphyRecent Advances in Stratigraphic and Sedimentologic Computer Simulations*; Society for Sedimentary Geology: Tulsa, OK, USA, 1999.
43. Sun, D.; Bloemendal, J.; Rea, D.K.; Vandenberghe, J.; Jiang, F.; An, Z.; Su, R. Grain-Size Distribution Function of Polymodal Sediments in Hydraulic and Aeolian Environments, and Numerical Partitioning of the Sedimentary Components. *Sediment. Geol.* **2002**, *152*, 263–277. [CrossRef]
44. Tsoar, H.; Pye, K. Dust transport and the question of desert loess formation. *Sedimentology* **1987**, *34*, 139–153. [CrossRef]
45. Shiling, Y.; Zhongli, D. Spatial Changes in Grain Size of Loess Deposits in the Chinese Loess Plateau and Implications for Palaeoenvironment. *Quat. Sci.* **2017**, *37*, 934–944.
46. Han, Y.; Fang, X.; Kang, S.; Wang, H.; Kang, F. Shifts of dust source regions over central Asia and the Tibetan Plateau: Connections with the Arctic oscillation and the westerly jet. *Atmos. Environ.* **2008**, *42*, 2358–2368. [CrossRef]
47. Újvári, G.; Kok, J.F.; Varga, G.; Kovács, J. The Physics of Wind-Blown Loess: Implications for Grain Size Proxy Interpretations in Quaternary Paleoclimate Studies. *Earth Sci. Rev.* **2016**, *154*, 247–278. [CrossRef]
48. Bronger, A.; Heinkele, T. Mineralogical and clay mineralogical aspects of loess research. *Quat. Int.* **1990**, *7–8*, 37–51. [CrossRef]
49. An, Z.; Kukla, G.J.; Porter, S.C.; Xiao, J. Magnetic susceptibility evidence of monsoon variation on the Loess Plateau of central China during the last 130,000 years. *Quat. Res.* **1991**, *36*, 29–36. [CrossRef]
50. Pye, K. The nature, origin and accumulation of loess. *Quat. Sci. Rev.* **1995**, *14*, 653–667. [CrossRef]
51. Prins, M.A. Glacial and Interglacial Eolian Dust Dispersal Patterns across the Chinese Loess Plateau Inferred from Decomposed Loess Grain-Size Records. *Geochem. Geophys. Geosyst.* **2007**, *8*, Q07Q05. [CrossRef]
52. Donghuai, S.; Chen, F.; Bloemendal, J.; Su, R. Seasonal Variability of Modern Dust over the Loess Plateau of China: Seasonal Variability of Dust in China. *J. Geophys. Res. Atmos.* **2003**, *108*, D21.
53. van der Does, M.; Knippertz, P.; Zschenderlein, P.; Harrison, R.G.; Stuut, J.-B.W. The mysterious long-range transport of giant mineral dust particles. *Sci. Adv.* **2018**, *4*, eaau2768. [CrossRef]
54. Pan, B.; Wang, J. Loess Record of Qinghai-Xizang Plateau Monsoon Variations in the Eastern Part of the Plateau since the Last Interglacial. *Quat. Sci.* **1999**, *19*, 330–335, (In Chinese with English abstract).
55. Sun, D.; Su, R.; Bloemendal, J.; Lu, H. Grain-Size and Accumulation Rate Records from Late Cenozoic Aeolian Sequences in Northern China: Implications for Variations in the East Asian Winter Monsoon and Westerly Atmospheric Circulation. *Palaeogeogr. Palaeoclimatol. Palaeoecol.* **2008**, *264*, 39–53. [CrossRef]
56. Wang, L.; Jia, J.; Zhao, H.; Liu, H.; Duan, Y.; Xie, H.; Zhang, D.D.; Chen, F. Optical Dating of Holocene Paleosol Development and Climate Changes in the Yili Basin, Arid Central Asia. *Holocene* **2019**, *29*, 1068–1077. [CrossRef]
57. Kohfeld, K.E.; Harrison, S.P. Glacial-Interglacial Changes in Dust Deposition on the Chinese Loess Plateau. *Quat. Sci. Rev.* **2003**, *22*, 1859–1878. [CrossRef]
58. Ting, C.; Yang, S.; Liu, W.; Li, S.; Liang, M.; Liu, N.; Chen, H. Characteristics and Paleoclimatic Significance of the Soil Bulk Density for the Loess Deposit from Ganzi Region, Western Sichuan Plateau. *J. Earth Environ.* **2018**, *9*, 230–237.
59. Kutzbach, J.E.; Guetter, P.J.; Behling, P.J.; Selin, R. Simulated Climatic Changes: Results of the Cohmap Climate-Model Experiments. In *Global Climates Since the Last Glacial Maximum*; University of Minnesota Press: Minneapolis, MN, USA, 1993.
60. Sun, D. Monsoon and Westerly Circulation Changes Recorded in the Late Cenozoic Aeolian Sequences of Northern China. *Glob. Planet. Chang.* **2004**, *41*, 63–80.
61. Lü, L.; Fang, X.; Lu, H.; Han, Y.; Yang, S.; Li, J.; An, Z. Millennial-scale climate change since the last glaciation recorded by grain sizes of loess deposits on the northeastern Tibetan Plateau. *Chin. Sci. Bull.* **2004**, *49*, 1157–1164. [CrossRef]
62. Vriend, M.; Prins, M.A.; Buylaert, J.-P.; Vandenberghe, J.; Lu, H. Contrasting dust supply patterns across the north-western Chinese Loess Plateau during the last glacial-interglacial cycle. *Quat. Int.* **2011**, *240*, 167–180. [CrossRef]
63. Liu, X.J.; Xiao, G.; Chongyi, E.; Li, X.; Lai, Z.; Yu, L.; Wang, Z. Accumulation and erosion of aeolian sediments in the northeastern Qinghai-Tibetan Plateau and implications for provenance to the Chinese Loess Plateau. *J. Asian Earth Sci.* **2017**, *135*, 166–174. [CrossRef]
64. Liu, L.; Yang, S.; Cheng, T.; Liu, X.; Luo, Y.; Liu, N.; Chen, H.; Chen, Z.; Li, P.; Liu, W. Chronology and dust mass accumulation history of the Wenchuan loess on eastern Tibetan Plateau since the last glacial. *Aeolian Res.* **2021**, *53*, 100748. [CrossRef]

65. Sime, L.C.; Kohfeld, K.E.; Le Quéré, C.; Wolff, E.W.; de Boer, A.M.; Graham, R.M.; Bopp, L. Southern Hemisphere westerly wind changes during the Last Glacial Maximum: Model-data comparison. *Quat. Sci. Rev.* **2013**, *64*, 104–120. [CrossRef]
66. Ding, Z.; Ranov, V.; Yang, S.; Finaev, A.; Han, J.; Wang, G. The loess record in southern Tajikistan and correlation with Chinese loess. *Earth Planet. Sci. Lett.* **2002**, *200*, 387–400. [CrossRef]
67. Wang, N.; Jiang, D.; Lang, X.M. Northern Westerlies During the Last Glacial Maximum: Results from Cmip5 Simulations. *J. Clim.* **2018**, *31*, 1135–1153. [CrossRef]
68. Laîné, A.; Kageyama, M.; Salas-Mélia, D.; Voldoire, A.; Rivière, G.; Ramstein, G.; Planton, S.; Tyteca, S.; Peterschmitt, J.Y. Northern Hemisphere Storm Tracks During the Last Glacial Maximum in the Pmip2 Ocean-Atmosphere Coupled Models: Energetic Study, Seasonal Cycle, Precipitation. *Clim. Dyn.* **2008**, *32*, 593–614. [CrossRef]
69. Chang, H.; An, Z.; Wu, F.; Song, Y.; Qiang, X.; Li, L. Late Miocene-early Pleistocene climate change in the mid-latitude westerlies and their influence on Asian monsoon as constrained by the K/Al ratio record from drill core Ls2 in the Tarim Basin. *Catena* **2017**, *153*, 75–82. [CrossRef]
70. Fang, X.; An, Z.; Clemens, S.C.; Zan, J.; Shi, Z.; Yang, S.; Han, W. The 3.6-Ma aridity and westerlies history over midlatitude Asia linked with global climatic cooling. *Proc. Natl. Acad. Sci. USA* **2020**, *117*, 24729–24734. [CrossRef]
71. Zhisheng, A.; Guoxiong, W.; Jianping, L.; Youbin, S.; Yimin, L.; Weijian, Z.; Yanjun, C.; Anmin, D.; Li, L.; Jiangyu, M.; et al. Global Monsoon Dynamics and Climate Change. *Annu. Rev. Earth Planet. Sci.* **2015**, *43*, 29–77. [CrossRef]
72. Liu, J.; Wang, R.; Zhao, Y.; Yang, Y. A 40,000-year record of aridity and dust activity at Lop Nur, Tarim Basin, northwestern China. *Quat. Sci. Rev.* **2019**, *211*, 208–221. [CrossRef]
73. Nottebaum, V.; Stauch, G.; Hartmann, K.; Zhang, J.; Lehmkuhl, F. Unmixed Loess Grain Size Populations Along the Northern Qilian Shan (China): Relationships between Geomorphologic, Sedimentologic and Climatic Controls. *Quat. Int.* **2015**, *372*, 151–166. [CrossRef]
74. Ruth, U.; Bigler, M.; Röthlisberger, R.; Siggaard-Andersen, M.-L.; Kipfstuhl, S.; Goto-Azuma, K.; Hansson, M.E.; Johnsen, S.J.; Lu, H.; Steffensen, J.P. Ice core evidence for a very tight link between North Atlantic and east Asian glacial climate. *Geophys. Res. Lett.* **2007**, *34*, L03706. [CrossRef]
75. Svensson, A.; Biscaye, P.E.; Grousset, F.E. Characterization of late glacial continental dust in the Greenland Ice Core Project ice core. *J. Geophys. Res. Atmos.* **2000**, *105*, 4637–4656. [CrossRef]
76. Újvári, G.; Klötzli, U.; Stevens, T.; Svensson, A.; Ludwig, P.; Vennemann, T.; Gier, S.; Horschinegg, M.; Palcsu, L.; Hippler, D.; et al. Greenland Ice Core Record of Last Glacial Dust Sources and Atmospheric Circulation. *J. Geophys. Res. Atmos.* **2022**, *127*, e2022JD036597. [CrossRef]
77. Wei, T.; Brahney, J.; Dong, Z.; Kang, S.; Zong, C.; Guo, J.; Yang, L.; Qin, X. Hf–Nd–Sr Isotopic Composition of the Tibetan Plateau Dust as a Fingerprint for Regional to Hemispherical Transport. *Environ. Sci. Technol.* **2021**, *55*, 10121–10132. [CrossRef]
78. Laskar, J.; Robutel, P.; Joutel, F.; Gastineau, M.; Correia, A.; Levrard, B. A long-term numerical solution for the insolation quantities of the Earth. *Astron. Astrophys.* **2004**, *428*, 261–285. [CrossRef]
79. Lisiecki, L.E.; Raymo, M.E. A Pliocene-Pleistocene Stack of 57 Globally Distributed Benthic Delta O-18 Records. *Paleoceanography* **2005**, *20*, PA1003.
80. Jouzel, J.; Alley, R.B.; Cuffey, K.M.; Dansgaard, W.; Grootes, P.; Hoffmann, G.; Johnsen, S.J.; Koster, R.; Peel, D.; Shuman, C.A.; et al. Validity of the temperature reconstruction from water isotopes in ice cores. *J. Geophys. Res. Ocean.* **1997**, *102*, 26471–26487. [CrossRef]
81. Bereiter, B.; Eggleston, S.; Schmitt, J.; Nehrbass-Ahles, C.; Stocker, T.F.; Fischer, H.; Kipfstuhl, S.; Chappellaz, J. Revision of the EPICA Dome C CO_2 record from 800 to 600 kyr before present. *Geophys. Res. Lett.* **2015**, *42*, 542–549. [CrossRef]
82. Ruddiman, W.F. Orbital Insolation, Ice Volume, and Greenhouse Gases. *Quat. Sci. Rev.* **2003**, *22*, 1597–1629. [CrossRef]
83. Berge, A. The Role of Co_2, Sea Level, and Vegetation During the Milankovitch-Forced Glacial-Interglacial Cycles. In *Geosphere-Biosphere Interactions and Climate*; Hammer, C.U., Bengtsson, L.O., Eds.; Cambridge University Press: Cambridge, UK, 2001; pp. 119–146.
84. Duan, F.; An, C.; Wang, W.; Herzschuh, U.; Zhang, M.; Zhang, H.; Liu, Y.; Zhao, Y.; Li, G. Dating of a late Quaternary loess section from the northern slope of the Tianshan Mountains (Xinjiang, China) and its paleoenvironmental significance. *Quat. Int.* **2020**, *544*, 104–112. [CrossRef]
85. Hou, K.; Qian, H.; Zhang, Y.T.; Zhang, Q.Y.; Qu, W.G. New insights into loess formation on the southern margin of the Chinese Loess Plateau. *Catena* **2021**, *204*, 105444. [CrossRef]
86. Jiang, H.C.; Wan, S.M.; Ma, X.L.; Zhong, N.; Zhao, D.B. End-member modeling of the grain-size record of Sikouzi fine sediments in Ningxia (China) and implications for temperature control of Neogene evolution of East Asian winter monsoon. *PLoS ONE* **2017**, *12*, 10. [CrossRef] [PubMed]
87. Kong, F.; Xu, S.; Han, M.; Chen, H.; Miao, X.; Kong, X.; Jia, G. Application of grain size endmember analysis in the study of dust accumulation processes: A case study of loess in Shandong Province, East China. *Sediment. Geol.* **2021**, *416*, 105868. [CrossRef]

88. Li, X.; Peng, T.; Ma, Z.; Li, M.; Li, P.; Feng, Z.; Guo, B.; Yu, H.; Ye, X.; Zhang, J.; et al. The Sources and Transport Dynamics of Eolian Sediments in the NE Tibetan Plateau Since 6.7 Ma. *Geochem. Geophys. Geosyst.* **2020**, *21*, e2019GC008682. [CrossRef]
89. Xu, Y.; Li, J.; Pan, F.; Yang, B.; Tang, Y.; Bi, Y.; Li, T.; Yue, L.; Wingate, M.T. Late Neogene aridification and wind patterns in the Asian interior: Insight from the grain-size of eolian deposits in Altun Shan, northern Tibetan Plateau. *Palaeogeogr. Palaeoclim. Palaeoecol.* **2018**, *511*, 532–540. [CrossRef]